Materials Characterization 195 (2023) 112489

Contents lists available at ScienceDirect

Materials Characterization

journal homepage: www.elsevier.com/locate/matchar

Enhancement of the corrosion properties of selective laser melted Co-Cr-Mo alloy by selective oxidation annealing

Hyeon-Tae Im [a,c], Dae Ha Kim [b], Bosung Seo [a], Jae-Young Park [a], Ki Beom Park [a,c], Da Hye Lee [a], Chan Bin Mo [a], Young Do Kim [c,*], Kwangsuk Park [a,*], Hyung-Ki Park [a,*]

[a] Functional Materials and Components R&D Group, Korea Institute of Industrial Technology, Gangneung 25440, Republic of Korea
[b] KONASOL R&D center, KONASOL, Dangjin 31806, Republic of Korea
[c] Division of Materials Science and Engineering, Hanyang University, Seoul 04763, Republic of Korea

ARTICLE INFO

Keywords:
Co-Cr-Mo alloy
Selective laser melting
Selective oxidation
Corrosion property

ABSTRACT

This study investigated the surface modification effect of the selective oxidation annealing (SOA) on the corrosion properties of cobalt-chromium-molybdenum (Co-Cr-Mo) alloy fabricated by selective laser melting (SLM). For the SOA, each element's oxidation driving force was calculated, and the condition in which only Cr was selectively oxidized was thermodynamically analyzed. The oxidation potential was controlled by the partial pressure ratio of hydrogen gas and water vapor, and the alloy samples were annealed following the condition of the selective oxidation of Cr. The changes in the oxide layer and corrosion properties according to the SOA time were examined. On the as-built sample's surface, a very thin native oxide film was formed. After the SOA, a dense chromium oxide (Cr_2O_3) layer was formed on the surface, and its thickness increased along with the SOA time. These changes in the oxide layer had an impact on corrosion properties. Even though all samples before and after the SOA were under the passivation state, the corrosion performances in terms of corrosion potential and corrosion current density were improved by the SOA. The electrochemical impedance spectroscopy (EIS) results further confirmed that the improved corrosion resistance mainly came from the increased oxide layer resistance (R_o) because of the thickened oxide layer.

1. Introduction

Cobalt-chromium-molybdenum (Co-Cr-Mo; CCM) alloy has high mechanical strength and wear resistance compared to titanium (Ti) alloys because of the precipitation of hard carbide phases. [1–3]. These characteristics make it widely used as biomedical implants that take on large loads and require high abrasion resistance, like an artificial hip joint [4,5]. However, the CCM alloy has low corrosion properties and biocompatibility compared to Ti alloys. In the CCM alloy, Co is eluted as an ion in a corrosive environment, and releasing a metal ion is toxic to cells and increases carcinogenesis risk [6–8].

Because the CCM alloy has low machinability due to its high hardness and hard carbide phases, fabricating parts using a conventional machining process is challenging [9–11]. By applying selective laser melting (SLM), a manufacturing process that selectively melts powders using a laser source, parts with complex internal structures and near-net shapes could be directly fabricated [12–15]. Therefore, research on manufacturing CCM alloy parts using the SLM process is being actively conducted.

In the SLM process, since the laser-formed melt pool rapidly cools, samples fabricated through such process have a refined microstructure and residual stress, resulting in higher mechanical properties than samples fabricated using the conventional casting method [16–19]. In addition, adopting the SLM process improves corrosion properties due to the formation of the uniform microstructure and the inhibition of the macrosegregation [20–22]. Indeed, Xin et al. [21] compared the corrosion properties of samples fabricated through SLM and the casting method and reported that the Co ion elution rate of the SLM sample was significantly lower than of the sample produced via the casting. Therefore, by applying the SLM process to the CCM alloy, there are advantages that not only the process can be simplified by direct fabrication of near-net-shape parts, but also the higher corrosion properties can be achieved.

Recently, studies on the surface treatment improving the corrosion resistance of the CCM alloy fabricated by the SLM have been conducted. Seo et al. [23] reported a study on plasma electrolytic polishing (PEP) to

* Corresponding author.
E-mail addresses: ydkim1@hanyang.ac.kr (Y. Do Kim), kpark63@kitech.re.kr (K. Park), mse03@kitech.re.kr (H.-K. Park).

https://doi.org/10.1016/j.matchar.2022.112489
Received 21 July 2022; Received in revised form 22 October 2022; Accepted 13 November 2022
Available online 17 November 2022

modify the surface properties of the selective laser melted CCM alloy. When the surface of the CCM alloy is polished through the PEP process, not only the roughness is effectively decreased, but also the corrosion resistance is improved by forming a dense Cr_2O_3 oxide layer on the alloy surface. In the CCM alloy, the Cr_2O_3 oxide layer acts as a barrier for dissolving Co and hinder the elution of Co ion from the alloy [6]. Therefore, the corrosion resistance can be improved if the PEP process is controlled to form a dense and thick Cr_2O_3 oxide layer on the alloy surface.

A selective oxidation annealing (SOA) technology has been developed to modify the surface oxide layer by selectively oxidizing a specific element in metallic alloys [24–26]. Park et al. [26] studied changing the composition of the oxide layer of iron-silicon-chromium (Fe-Si-Cr) alloy using the difference in the oxidation driving force of Fe, Si, and Cr. In particular, the heat treatment was performed under an atmosphere in which Fe was reduced, Si and Cr were selectively oxidized, and the oxidation potential was controlled by the partial pressure ratio of hydrogen gas and water vapor. The experiments reported that SiO_2 and Cr_2O_3 oxide layers with excellent corrosion resistance were densely formed on the alloy surface, improving the corrosion resistance.

Among the elements constituting the CCM alloy, Cr has the highest oxidation driving force. If a dense and thick Cr_2O_3 oxide layer can be formed on the surface through the SOA, it is possible to improve the corrosion resistance of the CCM alloy by the simple heat treatment method. Therefore, this study thermodynamically analyzed the possibility of selective oxidation of Cr in the CCM alloy. In addition, the changes in the surface oxide layer and the corrosion properties by the SOA were examined.

2. Experimental procedures

The CCM alloy powders fabricated by a vacuum induction gas atomization method were used as the initial material for this study. These alloy powders had a spherical morphology; their d10, d50, and d90 values were 24.9, 39.1, and 60.8 μm, respectively. In addition, the chemical composition was examined by an inductively coupled plasma mass spectrometry (OPTIMA 7300 DV, Perkin-Elmer). The composition of the powders was 28.5Cr-6.2Mo-0.2C-0.14N, which met the composition criteria of ASTM F75 [27].

The CCM bulk samples were prepared through the SLM process using Merain Co. Ltd.'s DAVID 1.0 Metal 3D printer. The laser spot size and hatching spaces were 40 and 60 μm, respectively. The laser power and scan speed were set to 300 W and 800 mm/s, respectively, while the layer thickness was 32 μm. The SLM samples were fabricated as cube-shaped with a size of 20 × 20 × 20 mm^3. For the SOA and evaluation of the corrosion properties, they were machined to a size of 15 × 15 × 3 mm^3 by electric discharge machining. The samples' surfaces were polished with SiC paper and 3-μm diamond suspension and cleaned through ethanol ultrasonication.

The SOA was carried out using a heat treatment furnace equipped with a thermostat water bath that controls the oxidation potential using the partial pressure ratio between hydrogen gas and water vapor ($p_{H_2(g)}/p_{H_2O(g)}$). The schematic of the furnace is shown in Fig. 1. Firstly, 100% H_2 gas with a flow rate of 1000 sccm was injected into the thermostat water bath. After bubbling H_2 gas in the water, the H_2-H_2O mixed gas flowed into the heat treatment furnace. The gas inlet line was heated to 50 °C using a heating band to prevent the water vapor from condensing. The water temperature in the thermostat bath was set to 20 °C. From the above condition, the $p_{H_2(g)}/p_{H_2O(g)}$ ratio was calculated to 41.8. The reason for controlling the $p_{H_2(g)}/p_{H_2O(g)}$ ratio to 41.8 will be explained in results and discussion section.

For the SOA, the heat treatment furnace was first heated to 650 °C, and the H_2-H_2O mixed gas flowed to the furnace for 1 h. Then, the samples were charged into the furnace through a load lock chamber and they were annealed at 650 °C for 10, 20, and 30 min. Hereafter, the samples applying the SOA for 10, 20, and 30 min will be designated as SOA10, SOA20, and SOA30, respectively. The samples were loaded back into the load lock chamber after finishing the holding time, and 100% dry H_2 gas was supplied during the cooling process.

The oxidation driving force with respect to the temperature of Co, Cr, and Mo was calculated by Thermo-Calc software using the condensed compound database of SSUB5. The standard Gibbs free energy change (ΔG^o) of solid-gas reactions was obtained from the standard Gibbs free energy (G^o) of each elements. The samples' surface properties before and after the SOA were analyzed using an X-ray photoelectron spectroscopy (XPS) (K-Alpha, Thermo Fisher). The thickness and chemical composition of the surface oxide layers on the samples were examined using a transmission electron microscope (TEM) (Titan G2 ChemiSTEM Cs Probe, FEI) equipped with energy-dispersive X-ray spectroscopy (EDS). The TEM samples were prepared using a focused ion beam (FIB) (Versa 3D DualBeam, FEI). The microstructures of the as-built and SOA30 samples were observed using a field emission-scanning electron microscope (FE-SEM) (QUANTA FEG 250, FEI) equipped with electron backscatter diffraction (EBSD) (DigiView, EDAX).

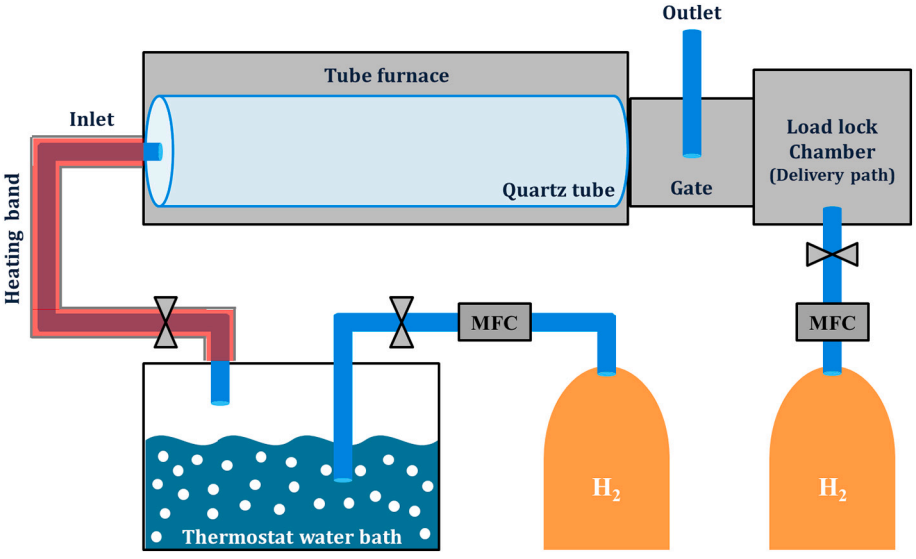

Fig. 1. Schematic diagram of the heat treatment furnace for the SOA. A 100% H_2 gas was bubbled in the water, and then H_2-H_2O mixed gas was supplied to the furnace.

All electrochemical tests to characterize corrosion properties were conducted with a three-electrode configuration cell, where platinum (Pt) and silver/silver chloride (Ag/AgCl) electrodes were used as counter and reference electrodes. After removing dissolved oxygen in 3.5 wt% sodium chloride (NaCl) solution by applying nitrogen (N_2) gas, open circuit potential (OCP), potentiodynamic polarization, and electrochemical impedance spectroscopy (EIS) were carried out. The polarization test was conducted with a scan rate of 0.05 mV/s from −1.5 V to 1.5 V, and the EIS test was conducted with an alternating current (AC) amplitude of 10 mV at 0.05 Hz to 10,000 Hz.

3. Results and discussion

For the SOA, the oxidation driving force of the elements constituting the CCM alloy was calculated using Thermo-Calc software. Fig. 2 represents the oxidation driving force of Co, Cr, and Mo. At 650 °C, the temperature at which the heat treatment was performed in this study, Cr has the highest oxidation driving force, and Co and Mo have the similar oxidation driving force value. Because Cr has a higher oxidation driving force than other elements, it will be possible to selectively oxidize Cr by controlling the oxidation potential to form a Cr_2O_3 oxide layer on the surface. Therefore, to form an atmosphere for the selective oxidation of Cr during the heat treatment, the $p_{H_2(g)}/p_{H_2O(g)}$ value in the equilibrium state of the oxidation and reduction ($(p_{H_2(g)}/p_{H_2O(g)})_{eq}$) was calculated.

The oxidation behavior of metallic elements is affected by the temperature and the oxygen partial pressure ($p_{O_2(g)}$), and when oxidation and reduction are in an equilibrium state, it can be expressed as the following equation.

$$\Delta G^o = RTln\left(p_{O_2(g)}\right)_{eq} \tag{1}$$

where ΔG^o is the standard Gibbs free energy change ($\Delta G^o = G^o_{MO_{2(s)}} - G^o_{M_{(s)}} - G^o_{O_{2(g)}}$), R is the gas constant, and $(p_{O_2(g)})_{eq}$ is the equilibrium oxygen partial pressure. The ΔG^o values were calculated using Thermo-Calc, and the ΔG^o values of Co, Cr, and Mo for the oxidation at 650 °C were − 338.2, −597.5, and − 335.5 kJ/mol, respectively. Substituting the ΔG^o values to Eq. (1), the $(p_{O_2(g)})_{eq}$ values for Co, Cr, and Mo at 650 °C were calculated to 1.6×10^{-16}, 1.2×10^{-34}, and 3.02×10^{-15} atm, respectively.

In the heat treatment process, if the $p_{O_2(g)}$ is controlled to be higher than the $(p_{O_2(g)})_{eq}$ value, the oxidation occurs; conversely, if the $p_{O_2(g)}$ is lower than the $(p_{O_2(g)})_{eq}$ value, the reduction occurs. Therefore, when

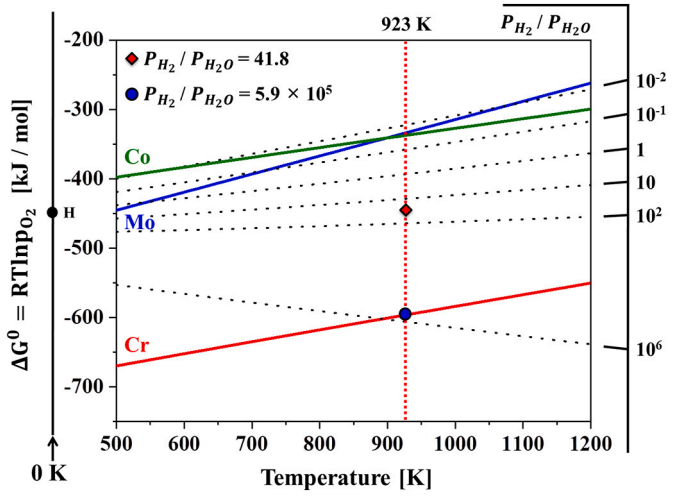

Fig. 2. Ellingham diagram for the oxidation of Co, Cr, and Mo. The oxidation driving force according to the temperature was calculated by Thermo-Calc software using the condensed compound database of SSUB5. The $p_{H_2(g)}/p_{H_2O(g)}$ values according to temperature were represented by the dotted lines.

$p_{O_2(g)}$ is controlled between 1.6×10^{-16} and 1.2×10^{-34} atm at 650 °C, it is possible to form an atmosphere in which Co and Mo are reduced while Cr is selectively oxidized. However, as the corresponding $p_{O_2(g)}$ for the selective oxidation of Cr is extremely low, forming the selective oxidation atmosphere in the CCM alloy by controlling the $p_{O_2(g)}$ was challenging.

The $(p_{O_2(g)})_{eq}$ can be substituted with the $(p_{H_2(g)}/p_{H_2O(g)})_{eq}$ through the oxidation reaction of H_2 gas as follows [25].

$$\Delta G = \Delta G^o_{H_2,oxidation} + 2RTlnp_{H_2O(g)} - 2RTlnp_{H_2(g)} - RTlnp_{O_2(g)} \tag{2}$$

where $\Delta G^o_{H_2\ oxidation}$ is the standard Gibbs free energy change for the oxidation of H_2 gas ($\Delta G^o_{H_2\ oxidation} = 2G^o_{H_2O(g)} - 2G^o_{H_2(g)} - G^o_{O_2(g)}$). ΔG is 0 in the equilibrium state for the oxidation reaction of H_2, and the Eq. (2) can be rearranged as follows.

$$RTlnp_{O_2(g)} = \Delta G^o_{H_2,oxidation} - 2RTln\left(\frac{p_{H_2(g)}}{p_{H_2O(g)}}\right) \tag{3}$$

With the mathematical rearrangement of Eq. (3), the equation for substituting the $p_{O_2(g)}$ to the $p_{H_2(g)}/p_{H_2O(g)}$ can be expressed as follows.

$$\frac{p_{H_2(g)}}{p_{H_2O(g)}} = exp\left\{\frac{\Delta G^o_{H_2,oxidation} - RTln\left(p_{O_2(g)}\right)}{2RT}\right\} \tag{4}$$

Reduction occurs when the $p_{H_2(g)}/p_{H_2O(g)}$ is higher than the $(p_{H_2(g)}/p_{H_2O(g)})_{eq}$ value, while oxidation occurs when the $p_{H_2(g)}/p_{H_2O(g)}$ is lower than the $(p_{H_2(g)}/p_{H_2O(g)})_{eq}$ value. The $(p_{H_2(g)}/p_{H_2O(g)})_{eq}$ values of Co, Cr, and Mo at 650 °C were calculated by substituting $(p_{O_2(g)})_{eq}$ values to Eq. (4), they were 4.19×10^{-1}, 5.93×10^5, and 5.55×10^{-1}, respectively. Therefore, if $p_{H_2(g)}/p_{H_2O(g)}$ is controlled between 4.19×10^{-1} and 5.93×10^5 at 650 °C, it is possible to form an atmosphere in which Co and Mo are reduced, and only Cr is selectively oxidized.

In this study, the H_2-H_2O mixed gas was supplied to the furnace by bubbling H_2 gas into the water. In the thermostat water bath, liquid water and water vapor are in an equilibrium state, and the $p_{H_2(g)}/p_{H_2O(g)}$ ratio can be controlled by the temperature of water temperature in the thermostat bath. The equation for the partial pressure of water vapor according to the water temperature in the thermostat bath can be expressed as follows [25,26].

$$p_{H_2O} = exp\left(-\frac{G^o_{H_2O(g)} - G^o_{H_2O(l)}}{RT}\right) \tag{5}$$

where $G^o_{H_2O(g)}$ and $G^o_{H_2O(l)}$ are the standard Gibbs free energy of water vapor and liquid water, respectively, which values were obtained from Thermo-Calc software. Since the experiments were carried out at 1 atm, the $p_{H_2(g)}$ value supplied to the furnace can be obtained by the following equation.

$$p_{H_2(g)} = 1 - p_{H_2O(g)} \tag{6}$$

The $p_{H_2(g)}/p_{H_2O(g)}$ value can be calculated according to the temperature of the thermostat bath using the above equations, and the results are summarized in Table 1.

For the SOA of Cr in the CCM alloy at 650 °C, the $p_{H_2(g)}/p_{H_2O(g)}$ should

Table 1
The $p_{H_2(g)}/p_{H_2O(g)}$ values with respect to the temperature of water in the thermostat bath when the 100% H_2 gas is bubbled.

Water temperature [°C]	p_{H_2O} [atm]	p_{H_2} [atm]	$\frac{p_{H_2(g)}}{p_{H_2O(g)}}$
10	0.012	0.988	80.4
20	0.023	0.977	41.8
30	0.042	0.958	22.6
40	0.074	0.926	12.6
50	0.123	0.877	7.13
60	0.198	0.802	4.04

be controlled between 4.19×10^{-1} and 5.93×10^{5}. Based on Table 1, if 100% H_2 gas is bubbled into the thermostat water bath at 20 °C, an atmosphere with the $p_{H_2(g)}/p_{H_2O(g)}$ value of 41.8 can be formed, which is a condition for the selective oxidation of Cr. Therefore, the experiments were carried out under the condition of the $p_{H_2(g)}/p_{H_2O(g)}$ value of 41.8 because not only Cr can selectively oxide but also the thermostat's temperature could maintain near room temperature. As described earlier, although the oxidation potential can be controlled by $p_{O_2(g)}$, there is a difficulty in controlling the $p_{O_2(g)}$ with an extremely low value. However, if the oxidation potential is controlled by the $p_{H_2(g)}/p_{H_2O(g)}$, an atmosphere for the selective oxidation can be formed more easily under realistic conditions.

The samples' surfaces were analyzed through XPS to inspect the surface oxide layer changes by the SOA. Fig. 3 shows the XPS results of the as-built, SOA10, SOA20, and SOA30 samples. In the XPS spectrum of the as-built sample, peaks with high intensity were presented at 778.2 and 793.2 eV, corresponding to the metallic state of Co (Co^0), and peaks with low intensity were also observed at 780 and 795.2 eV, corresponding to Co^{2+} oxidation state (Co $2p_{1/2}$ and Co $2p_{3/2}$) [28]. In the Cr region, peaks attributed to the metallic state of Cr (Cr^0) were detected at 574.9 and 584.4 eV, and peaks attributed to the Cr^{3+} oxidation state (Cr $2p_{3/2}$ and Cr $2p_{1/2}$) were detected at 576.6 and 586.3 eV [29]. In the Mo region, only metallic state peaks of Mo (Mo^0) at 228.1 and 231.3 eV were presented [30]. The surface analysis result of the as-built sample showed that the metallic state peaks produced by bulk metal were stronger than the ion state peaks from the oxide. Only a native oxide film was formed on the surface in the as-built sample as no additional heat treatment was applied. Therefore, the metallic state peaks are mainly observed in the XPS spectrum due to the thinness of the native oxide layer.

In the XPS spectra of the samples after the SOA (SOA10, SOA20, and SOA30), no peaks were observed in Co and Mo regions. In the Cr region, Cr^0 peaks disappeared, and the intensity of Cr^{3+} peaks at 576.6 and 586.3 eV drastically increased. Also, a peak formed by the multiplet splitting of the Cr^{3+} ion state is observed at 575.4 eV, slightly to the left side of the Cr $2p_{3/2}$ peak (576.6 eV) [31]. These results confirmed that only Cr was selectively oxidized under the condition with the $p_{H_2(g)}/p_{H_2O(g)}$ of 41.8, as in the thermodynamic calculation results, resulting in the formation of the Cr oxide layer on the surface.

Meanwhile, Fig. 4 shows the morphology of the oxide layer on the samples' surfaces observed using TEM. Only a very thin native oxide film was observed on the surface of the as-built sample, which affected the formation of the metallic state peaks with high intensity in the XPS result. The surface oxide layer's thickness increased with the SOA time, and the oxide layer thicknesses of SOA10, SOA20, and SOA30 samples

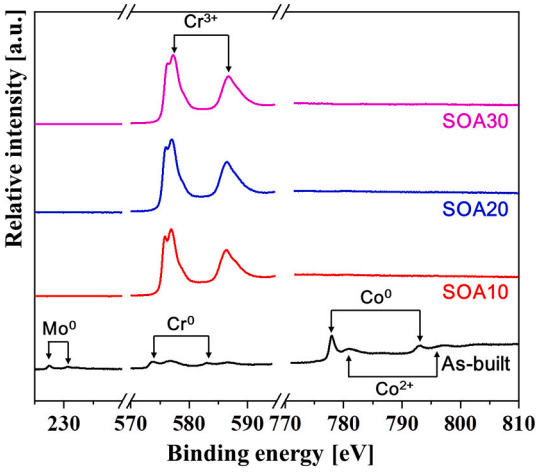

Fig. 3. X-ray photoelectron spectroscopy (XPS) spectra of the as-built, SOA10, SOA20, and SOA30 samples.

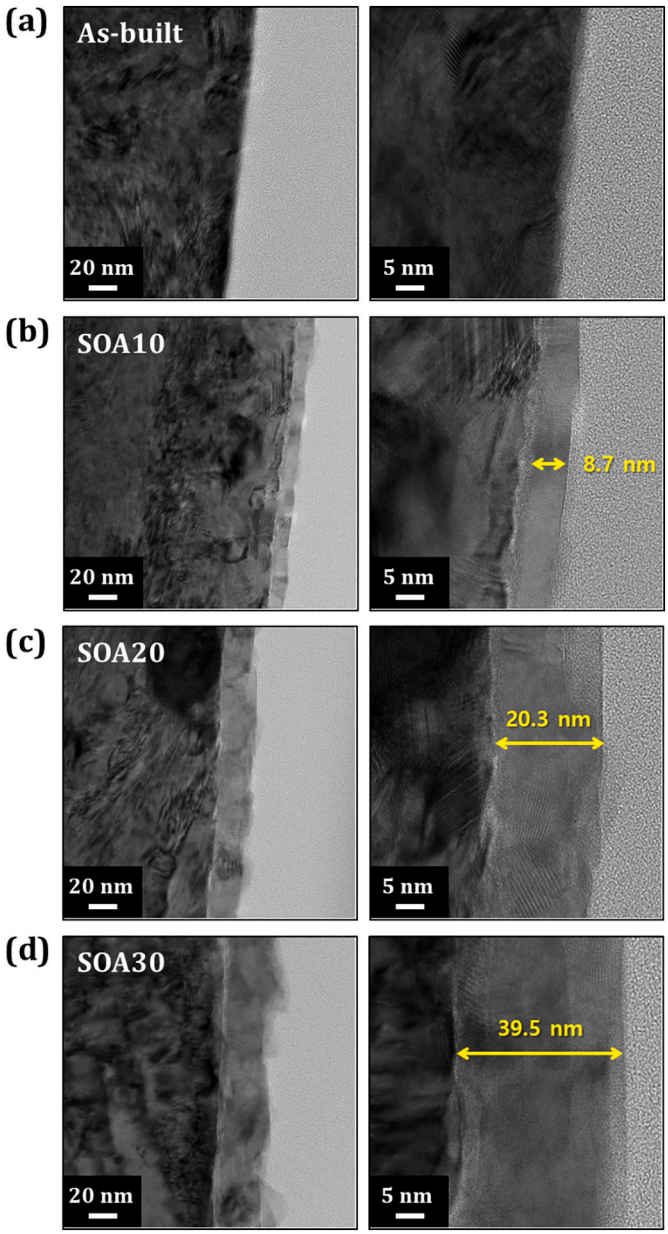

Fig. 4. Morphology of oxide layer on the (a) as-built, (b) SOA10, (c) SOA20, and (d) SOA30 samples analyzed by TEM.

were 8.7, 20.3, and 39.5 nm, respectively.

In addition, Fig. 5 represents the composition mapping results of the samples analyzed by the TEM. The oxide layer on the as-built sample was so thin that the area with high oxygen concentration could not be observed on the surface. On the surface of the SOA10, SOA20, and SOA30 samples, oxide layers with high Cr concentrations were formed by the SOA. The compositions of the surface oxide layers of the three samples were analyzed by the EDS, and the oxide layers of the samples had a similar composition with the Cr_2O_3. These XPS and TEM results confirmed that the Cr_2O_3 oxide layer could be formed on the surface through the SOA in the CCM alloy, and a thicker oxide layer could be obtained by increasing the annealing time.

Corrosion properties could be affected by the microstructure of the samples. Therefore, the microstructures of the as-built and SOA30 samples were observed by the EBSD and the result is shown in Fig. 6. In the as-built sample, an elongated microstructure formed along the building direction, which is the common microstructural feature of the sample fabricated by the SLM. The SOA30 sample had almost the same

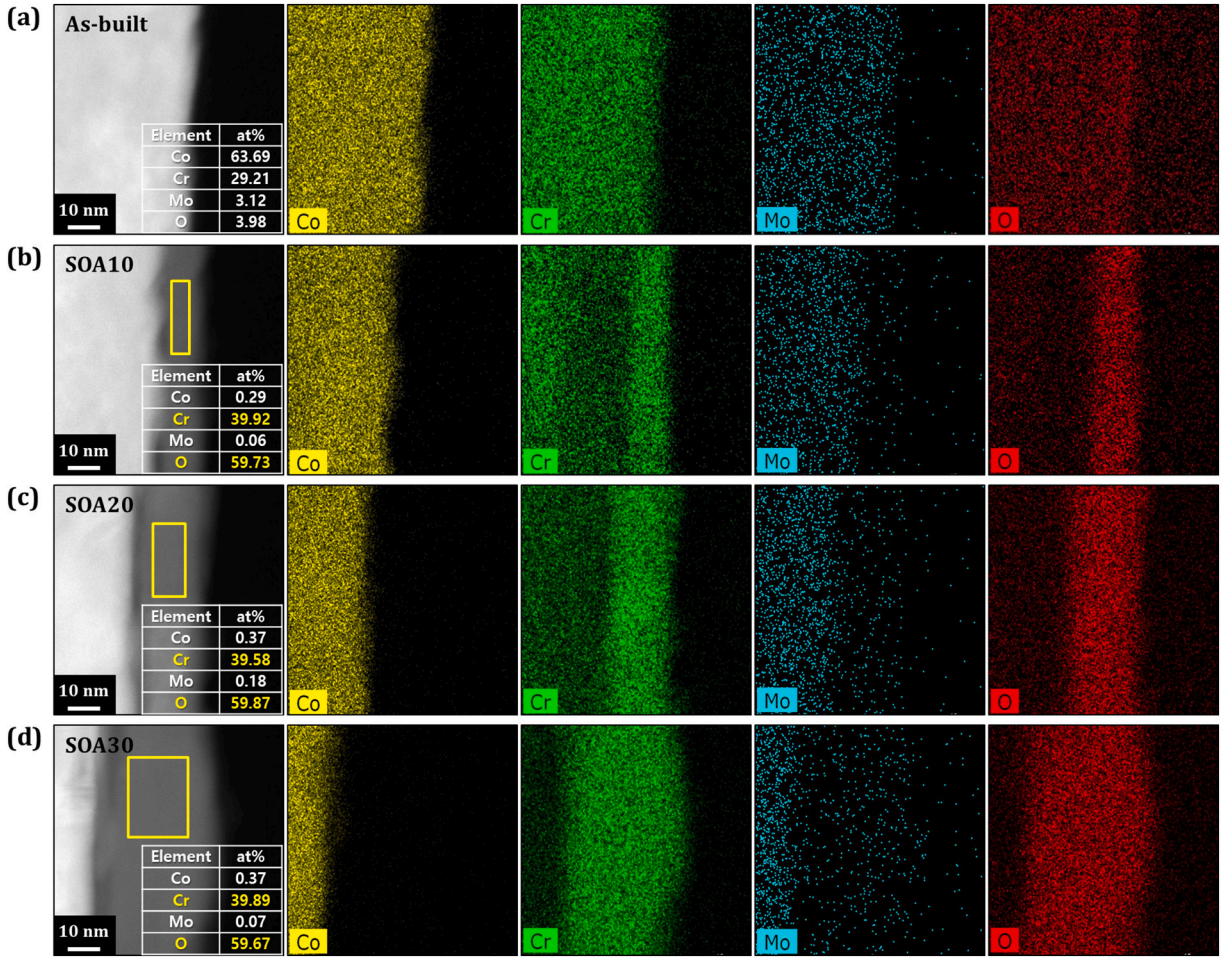

Fig. 5. Composition mapping results of the (a) as-built, (b) SOA10, (c) SOA20, and (d) SOA30 samples analyzed by TEM. The yellow rectangles indicate the region where the composition analysis of the oxide layer was performed. (For interpretation of the references to colour in this figure legend, the reader is referred to the web version of this article.)

microstructure as the as-built sample. From the microstructure observation, it was confirmed that the microstructure of the samples was not changed in the SOA performed in this study.

Fig. 7(a) and (b) represent OCP analysis results and polarization curves, respectively. The corrosion potential (E_{corr}) and corrosion current density (I_{corr}) derived from the polarization curves were summarized in Table 2. In Fig. 7(a), the OCP values of the sample increased with time elision in the initial stage. Once samples (electrode) were immersed in an electrolyte, the system tends to stabilize from the disturbance. The rise in the OCPs at the initial stage of the immersion is a kind of stabilization behavior. This stabilization would be achieved by surface reactions such as surface oxidation/reduction, surface dissolution/precipitation, and ion adsorption even though all samples are in the passivation state. This kind of rise in OCP was also reported in the previous study [23].

As shown in Fig. 7, the Cr_2O_3 oxide layer grown by the SOA altered the CCM alloy's corrosion properties. The OCP value shifted cathodically after the SOA, but no additional shift occurred with the annealing time. The OCP fluctuation shown in the as-built sample seemed to be ascribed to the very thin Cr_2O_3 oxide layer, so the fluctuation weakened and/or disappeared after the SOA due to the thickened oxide layer. From the OCP positions, it is known that all samples were well passivated, as shown in Fig. 7(b). However, because of the thickened oxide layer through the SOA, the corrosion current density remarkably decreased with the increase in corrosion potential. Further reduction in the corrosion current density occurred with the increase in the SOA time from 10 to 20 min. However, no additional reduction occurred when the annealing time increased from 20 to 30 min.

The EIS results also showed similar behavior to the polarization ones. Fig. 8 showed the evolutions of Nyquist plots with the SOA and its time, and the corresponding fitted data were listed in Table 3. The equivalent circuit used to fit consisted two resistor-capacitor (RC) cells connecting in the series, where R_{ct} and CPE_{dl} corresponded to a charge transfer resistance and double-layer capacitance at the oxide/electrolyte interface, and R_o and CPE_o were the resistance and capacitance of the oxide layer, respectively. Diameter of the semicircle denoting corrosion resistance was increased with the SOA as a result of the thickened oxide layer, but this increase stopped over the 20 min SOA. The main contribution to the increase in the corrosion resistance came from the resistance of the oxide layer (R_o), meaning that the increased oxide thickness played the main role in improving the corrosion resistance. For the oxide layer's resistance, the as-built sample had about 5×10^4 Ω•cm^2 and its value increased up to 1×10^6 Ω•cm^2 when the SOA over 20 min was applied.

4. Conclusions

The SOA successfully modified the surface of the CCM alloy fabricated by the SLM. Only Cr was selectively oxidized by annealing at 650 °C in an atmosphere with the $p_{H_2(g)}/p_{H_2O(g)}$ ratio of 41.8. In the as-built sample, a very thin native oxide film was formed on the surface. Through the XPS and TEM analyses, it was confirmed that the dense

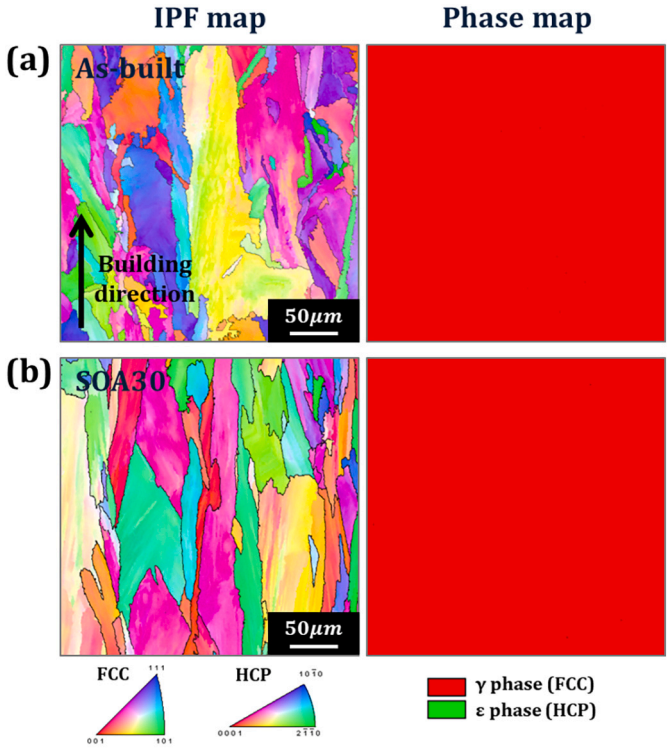

Fig. 6. Microstructure of the (a) as-built and (b) SOA30 samples observed by the EBSD.

Cr_2O_3 oxide layers were formed on the surface by the SOA. The thickness of the oxide layer steadily increased with extending SOA time, and the Cr_2O_3 oxide layer with a thickness of 39.5 nm was formed after the annealing for 30 min. The thickened oxide layer caused not only the ennoblement of the corrosion potential but also the reduction of the corrosion current density. In addition, the EIS results revealed that the improved corrosion resistance mainly came from the oxide layer's resistance which increased with the oxide layer's thickness.

Declaration of Competing Interest

The authors declare that they have no known competing financial interests or personal relationships that could have appeared to influence the work reported in this paper.

Table 2
Results of corrosion potential (E_{corr}) and corrosion current density (I_{corr}) were derived from the polarization curves of the as-built, SOA10, SOA20, and SOA30 samples.

	As-built	SOA10	SOA20	SOA30
E_{corr} (V)	−0.61	−0.25	−0.23	−0.22
I_{corr} (A/cm^2)	5.34×10^{-6}	2.84×10^{-7}	1.58×10^{-7}	1.30×10^{-7}

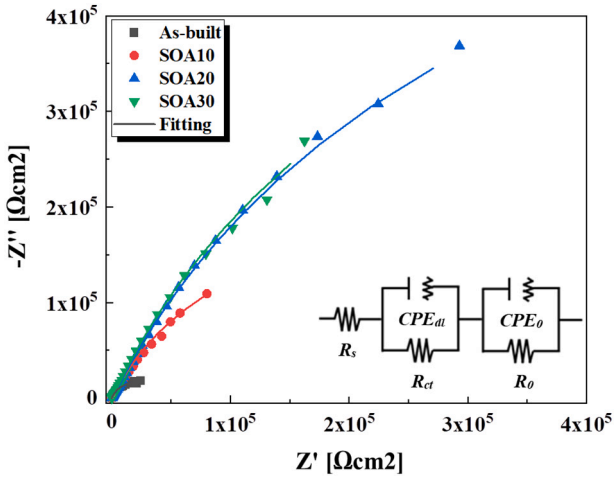

Fig. 8. Nyquist plots of the as-built, SOA10, SOA20, and SOA30 samples were measured in 3.5 wt% sodium chloride (NaCl) solutions. The inlet is the equivalent circuit used to interpret the data.

Table 3
Results of impedance parameters of the as-built, SOA10, SOA20, and SOA30 samples derived from the equivalent circuit analysis. The n is *CPE* dimensionless exponent.

Element	R_s	R_0	CPE_0 (n)	R_{ct}	CPE_{dl} (n)
As-built	9.241	5.15×10^4	3.05×10^{-5} (0.8807)	1011	9.25×10^{-5} (0.8045)
SOA10	9.774	4.50×10^5	1.63×10^{-5} (0.8707)	1016	4.85×10^{-5} (0.8358)
SOA20	9.214	1.39×10^6	4.69×10^{-6} (0.8822)	1021	4.58×10^{-6} (0.8424)
SOA30	9.415	1.32×10^6	7.81×10^{-6} (0.8853)	1018	1.82×10^{-5} (0.8451)

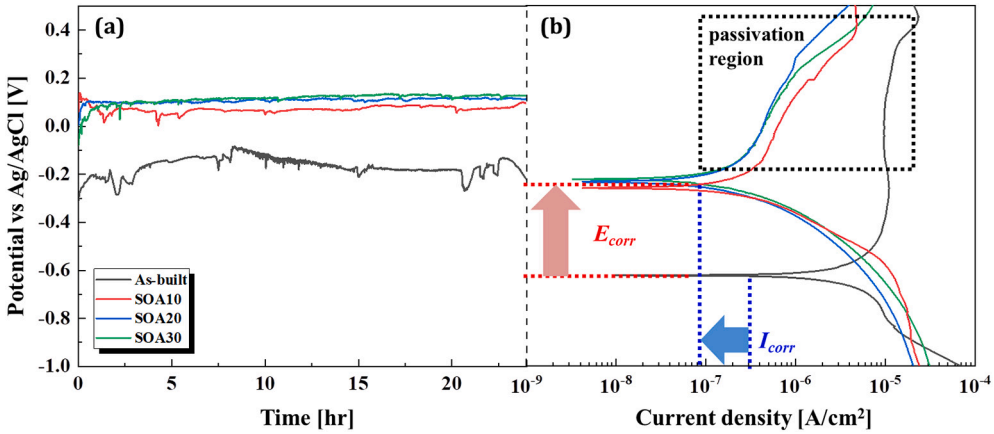

Fig. 7. (a) OCP variations with time and (b) polarization curves of the as-built, SOA10, SOA20, and SOA30 samples in 3.5 wt% sodium chloride (NaCl) solution.

Data availability

No data was used for the research described in the article.

Acknowledgments

This research was supported by the Korea Institute of Industrial Technology (KITECH JA-22-0010) and the Creative Materials Discovery Program (No. NRF-2019M3D1A1079227) through the National Research Foundation of Korea (NRF) funded by Ministry of Science and ICT.

References

[1] H.T. Im, H.S. Kang, H.G. Kang, H.Y. Kim, J. Choi, K.B. Park, T.W. Lee, C.B. Mo, H. K. Park, Effect of internal pores on tensile properties of Co-Cr-Mo alloy fabricated by selective laser melting, Rapid Prototyp. J. 28 (2) (2022) 404–408, https://doi.org/10.1108/RPJ-02-2021-0030.

[2] X.P. Tan, P. Wang, Y. Kok, W.Q. Toh, Z. Sun, S.M.L. Nai, M. Descoins, D. Mangelinck, E. Liu, S.B. Tor, Carbide precipitation characteristics in additive manufacturing of Co-Cr-Mo alloy via selective electron beam melting, Scr. Mater. 143 (2018) 117–121, https://doi.org/10.1016/j.scriptamat.2017.09.022.

[3] A. Takaichi, Y. Kajima, N. Kittikundecha, H.L. Htat, H.H.W. Cho, T. Hanawa, T. Yoneyama, N. Wakabayashi, Effect of heat treatment on the anisotropic microstructural and mechanical properties of Co–Cr–Mo alloys produced by selective laser melting, J. Mech. Behav. Biomed. Mater. 102 (2020), 103496, https://doi.org/10.1016/j.jmbbm.2019.103496.

[4] B. Qiana, K. Saeidi, L. Kvetková, F. Lofaj, C. Xiao, Z. Shen, Aginagalde, defects-tolerant Co-Cr-Mo dental alloys prepared by selective laser melting, Dent. Mater. 31 (2015) 1435–1444, https://doi.org/10.1016/j.dental.2015.09.003.

[5] S.H. Sun, Y. Koizumi, S. Kurosu, Y.P. Li, H. Matsumoto, A. Chiba, Build direction dependence of microstructure and high-temperature tensile property of Co–Cr–Mo alloy fabricated by electron beam melting, Acta Mater. 64 (2014) 154–168, https://doi.org/10.1016/j.actamat.2013.10.017.

[6] J.H. Hong, F.Y. Yeoh, Mechanical properties and corrosion resistance of cobalt-chrome alloy fabricated using additive manufacturing, Mater. Today: Proc. 29 (2020) 196–201, https://doi.org/10.1016/j.matpr.2020.05.543.

[7] X.Z. Xin, N. Xiang, J. Chen, B. Wei, In vitro biocompatibility of Co–Cr alloy fabricated by selective laser melting or traditional casting techniques, Mater. Lett. 88 (2012) 101–103, https://doi.org/10.1016/j.matlet.2012.08.032.

[8] T. Aldhohrah, J. Yang, J. Guo, H. Zhang, Y. Wang, Ion release and biocompatibility of Co-Cr alloy fabricated by selective laser melting from recycled Co-Cr powder: an in vitro study, J. Prosthet. Dent. 13 (2021), https://doi.org/10.1016/j.prosdent.2021.09.003.

[9] H.T. Im, D.H. Kim, Y.D. Kim, J.O. Fadonougbo, C.B. Mo, J.Y. Park, K.B. Park, J. W. Kang, H.S. Kang, H.K. Park, Effect of phase transformation on the mechanical properties of the Co-Cr-Mo alloy fabricated by selective laser melting, Mater. Charact. 186 (2022), 111767, https://doi.org/10.1016/j.matchar.2022.111767.

[10] L.H.M. Antunes, J.J. Hoyos, E.B. Fonseca, M. Béreš, P.F. da Silva Farina, E.S. N. Lopes, A.L. Jardini, R. Maciel Filho, Effect of phase transformation on ductility of additively manufactured Co–28Cr–6Mo alloy: an in situ synchrotron X-ray diffraction study during mechanical testing, Mater. Sci. Eng. A 764 (2019), 138262, https://doi.org/10.1016/j.msea.2019.138262.

[11] S.H. Sun, Y. Koizumi, S. Kurosu, Y.P. Li, A. Chiba, Phase and grain size inhomogeneity and their influences on creep behavior of Co–Cr–Mo alloy additive manufactured by electron beam melting, Acta Mater. 86 (2015) 305–318, https://doi.org/10.1016/j.actamat.2014.11.012.

[12] T.W. Na, W.R. Kim, S.M. Yang, O.H. Kwon, J.M. Park, G.H. Kim, K.H. Jung, C. W. Lee, H.K. Park, H.G. Kim, Effect of laser power on oxygen and nitrogen concentration of commercially pure titanium manufactured by selective laser melting, Mater. Charact. 143 (2018) 110–117, https://doi.org/10.1016/j.matchar.2018.03.003.

[13] W.H. Lee, T.W. Na, K.W. Yi, S.M. Yang, J.W. Kang, H.G. Kim, H.K. Park, Thermodynamic analysis of oxidation during selective laser melting of pure titanium, Rapid Prototyp. J. 26/8 (2020) 1401.

[14] H.K. Park, Y.K. Ahn, B.S. Lee, K.H. Jung, C.W. Lee, H.G. Kim, Refining effect of electron beam melting on additive manufacturing of pure titanium products, Mater. Lett. 187 (2017) 98–100, https://doi.org/10.1016/j.matlet.2016.10.065.

[15] H.K. Park, T.W. Na, S.M. Yang, G.H. Kim, B.S. Lee, H.G. Kim, Thermodynamic analysis of oxygen refining during electron-beam additive manufacturing of pure titanium products, Mater. Lett. 236 (2019) 106–108, https://doi.org/10.1016/j.matlet.2018.10.083.

[16] D. Wei, A. Anniyaer, Y. Koizumi, K. Aoyagi, M. Nagasako, H. Kato, A. Chiba, On microstructural homogenization and mechanical properties optimization of biomedical Co-Cr-Mo alloy additively manufactured by using electron beam melting, Addit. Manuf. 28 (2019) 215–227.

[17] Y. Liu, Y. Yang, D. Wang, A study on the residual stress during selective laser melting (SLM) of metallic powder, Int. J. Adv. Manuf. Technol. 87 (2016) 647–656.

[18] Y. Lu, S. Wu, Y. Gan, T. Huang, C. Yang, L. Junjie, J. Lin, Study on the microstructure, mechanical property and residual stress of SLM Inconel-718 alloy manufactured by differing island scanning strategy, Opt. Laser Technol. 75 (2015) 197–206, https://doi.org/10.1016/j.optlastec.2015.07.009.

[19] C. Cai, X. Wu, W. Liu, W. Zhu, H. Chen, J.C.D. Qiu, C.N. Sun, J. Liu, Q. Wei, Y. Shi, Selective laser melting of near-α titanium alloy Ti-6Al-2Zr-1Mo-1V: parameter optimization, heat treatment and mechanical performance, J. Mater. Sci. Technol. 57 (2020) 51–64, https://doi.org/10.1016/j.jmst.2020.05.004.

[20] S. Sun, Q. Teng, Y. Xie, T. Liu, R. Ma, J. Bai, C. Cai, Q. Wei, Two-step heat treatment for laser powder bed fusion of a nickel-based superalloy with simultaneously enhanced tensile strength and ductility, Addit. Manuf. 46 (2021), 102168, https://doi.org/10.1016/j.addma.2021.102168.

[21] X. Xin, J. Chen, N. Xiang, B. Wei, Surface properties and corrosion behavior of Co–Cr alloy fabricated with selective laser melting technique, Cell Biochem. Biophys. 67 (2013) 983–990, https://doi.org/10.1007/s12013-013-9593-9.

[22] Y. Kajima, A. Takaichi, N. Kittikundecha, H.L. Htat, H.H.W. Cho, Y. Tsutsumi, T. Hanawa, N. Wakabayashi, T. Yoneyam, Reduction in anisotropic response of corrosion properties of selective laser melted Co–Cr–Mo alloys by post-heat treatment, Dent. Mater. 37 (2021) e98–e108, https://doi.org/10.1016/j.dental.2020.10.020.

[23] B.S. Seo, H.K. Park, H.G. Kim, W.R. Kim, K.S. Park, Corrosion behavior of additive manufactured CoCr parts polished with plasma electrolytic polishing, Surf. Coat. Technol. 406 (2021), 126640, https://doi.org/10.1016/j.surfcoat.2020.126640.

[24] J.Y. Park, K.S. Park, B.S. Seo, J.O. Fadonougbo, T.W. Na, K.B. Park, H.T. Im, N. M. Hwang, H.K. Park, Insulation coating of Fe–Si–Cr soft magnetic powder by selective oxidation, Met. Mater. Int. 28 (2022) 1778–1782, https://doi.org/10.1007/s12540-021-01062-y.

[25] J.Y. Park, K.S. Park, J.O. Fadonougbo, K.R. Jang, S.D. Park, C.S. Park, C.B. Mo, N. M. Hwang, H.K. Park, Enhancement of the magnetic properties of Fe-Si-Cr soft magnetic composite by selective oxidation annealing, J. Magn. Magn. Mater. 561 (2022), 169697, https://doi.org/10.1016/j.jmmm.2022.169697.

[26] J.Y. Park, N.M. Hwang, B.S. Seo, H.T. Im, K.B. Park, C.S. Park, C.B. Mo, H.K. Park, K.S. Park, Study on surface modification of Fe–Si–Cr alloy by selective oxidation heat treatment and its corrosion properties, Steel Res. Int. 2200236 (2022), https://doi.org/10.1002/srin.202200236.

[27] T.J. Fleming, A. Kavanagh, G. Duggan, The effect of melt temperature on the mechanical properties of cast ASTM F75 CoCrMo alloy as explained by nitrogen and oxygen content, J. Mater. Res. Technol. 9 (2020) 9479–9486, https://doi.org/10.1016/j.jmrt.2020.06.079.

[28] E.A.A. Aboelazm, G.A.M. Ali, K.F. Chong, Cobalt oxide supercapacitor electrode recovered from spent Lithium-ion battery, Chem. Adv. Mater. 3 (4) (2018) 67–74.

[29] Z. Wang, L. Xi, Y. Yang, Y. Li, X. Han, Y. Zuo, J. Wang, Spin-dependent transport properties of CrO_2 Micro rod, Nano-Micro Lett. 6 (4) (2014) 365–371.

[30] E. Vernickaitė, M. Lelis, N. Tsyntsaru, V. Pakštas, H. Cesiulis, XPS studies on the Mo oxide-based coatings electrodeposited from highly saturated acetate bath, Chemija 31 (2020) 203–209, https://doi.org/10.6001/chemija.v31i4.4317.

[31] B.P. Payne, M.C. Biesinger, N.S. McIntyre, X-ray photoelectron spectroscopy studies of reactions on chromium metal and chromium oxide surfaces, J. Electron Spectrosc. Relat. Phenom. 184 (2011) 29–37, https://doi.org/10.1016/j.elspec.2010.12.001.